Efficient and Collision-Free Anticipative Cruise Control in Randomly Mixed Strings

R. Austin Dollar, *Student Member, IEEE* Ardalan Vahidi, *Member, IEEE*

***Abstract*—Connected intelligent vehicle following can improve safety and efficiency compared to today's road transport, but real traffic in the near future will not provide an ideal setting for its deployment. Unconnected human-driven vehicles will follow variable behavior patterns that combine with differences in dynamic capability to create heterogeneous scenarios. In this paper, connected automated vehicles employ model predictive control for following in traffic that may include both heavy and passenger vehicles at quasi-random positions. Adding further realism, some quasi-randomly mixed vehicles are completely unconnected and equipped with the reactive Intelligent Driver Model using pseudorandom parameters. A mixed-integer quadratic programming formulation adapts the predictive algorithm to diverse powertrain operating point constraints. The preceding vehicle's control input is estimated from velocity and brake light observations and used to probabilistically generate a preview for the ego vehicle. A terminal constraint designed using particle kinematics prevents collisions due to shortsightedness. Results are simulated at various heavy and predictive vehicle concentrations in the presence of packet loss. Linear fuel economy improvements between 1.4 % and 1.9 % per 10 % increase in predictive vehicle penetration rate are shown.**

***Index Terms*—Autonomous vehicles, control and optimization, intelligent vehicles, advanced cruise control, Probability modeling, traffic simulation.**

I. Introduction

AUTOMATED driving holds the potential to exceed human cognition and reshape the manner in which vehicles move and interact with infrastructure. Extracting maximum benefit from this technology will require not only reliable sensing and classification, but employment of the results in a safe, energy-efficient, and occupant-pleasing manner. Risk, inconsistency, and limited knowledge in human drivers lead to collisions that, in the United States, amounted to 1.6 % of gross domestic product in 2010 [1]. More importantly, over 37,000 people in the U.S [2]. and 25,500 in the E.U. [3] lost their lives to traffic collisions in 2016. Vehicle-to-vehicle (V2V) connectivity could potentially have impacted the 42% of such collisions in 2015 that involved more than one vehicle [4].

Commercial advanced driver assistance and semi-autonomous driving systems are advancing rapidly, but challenges remain. Current production systems often use a user-adjustable headway [5] rather than one that is optimized for collision avoidance, smoothness, or efficiency. Slow or delayed response sometimes irritates customers [6] and can even contribute to collisions [7]. A 2016 collision with an autonomous vehicle at-fault occurred because of a risky decision made based on incorrect anticipation [8]. Another more serious crash involved unsafe operation by a human driver [9]. Such incidents suggest that automated vehicle controls must not only prevent unsafe decisions by the host vehicle, but also protect against the potential actions of others.

Vehicles also affect the finances and well-being of the their users via energy consumption. In the case of combustion vehicles and electric vehicles (EVs) that rely on hydrocarbons for electricity, energy use promotes harmful emissions and consumption of typically nonrenewable resources. Particulate emissions damage human health and can affect life expectancy by whole years [10]. Despite this incentive to the contrary, the demand for motorized transport is so great that total miles driven in the U.S. continues to trend upward [11]. Hence, efficient implementation of such transport elements makes up an irreplaceable piece of energy security and sustainability. Powertrain improvements, lightweighting, and other passive technological trends can improve efficiency, but they do not affect wasteful traffic phenomena like phantom traffic jams. These events cause excessive energy dissipation as heat during braking while frustrating and disturbing occupants. While some eco-driving techniques such as pulse-and-glide could negatively impact traffic flow [12], automated driving in general can improve it.

Indeed, a prior study by Stern et al. showed string stability benefits in a ring-road experiment when automated car-following algorithms were used, even at low penetration rates [13]. These encouraging results using reactive control techniques motivate investigation of possibilities from anticipation. Simulation studies support the results of Stern et al. For example, [14] considers nonidealities such as communication delay, packet loss, and powertrain nonlinearities in the context of reactive gain-based control. This work will consider actuation nonlinearities and practical powertrain limitations in the context of model predictive control (MPC). Zheng and Vahidi [15] applied model predictive control to car following and Kamal [16] demonstrated attenuation of phantom traffic jams using MPC in simulation. In comparison to such prior work, this paper will adapt an MPC-based algorithm for highly heterogeneous vehicles and realistically pseudorandom surrounding driver behavior. Shortsightedness and difficulty in proving stability sometimes limit finite-horizon MPC, but these issues have been addressed for similar applications by Lefèvre et al. [17] and Dunbar et al. [18] respectively. Magdici and Althoff [19] approached collision-free guarantees with a two-controller method. The collision avoidance technique presented here is a simple alternative to [19] that uses a single controller rather than distinct nominal and emergency ones.

Compared to classical controllers, MPC has the advantage of naturally incorporating preview into its control decisions.

R. A. Dollar (corresponding author, rdollar@clemson.edu) and A. Vahidi (avahidi@clemson.edu) are with the Department of Mechanical Engineering, Clemson University, Clemson, SC 29634 USA.

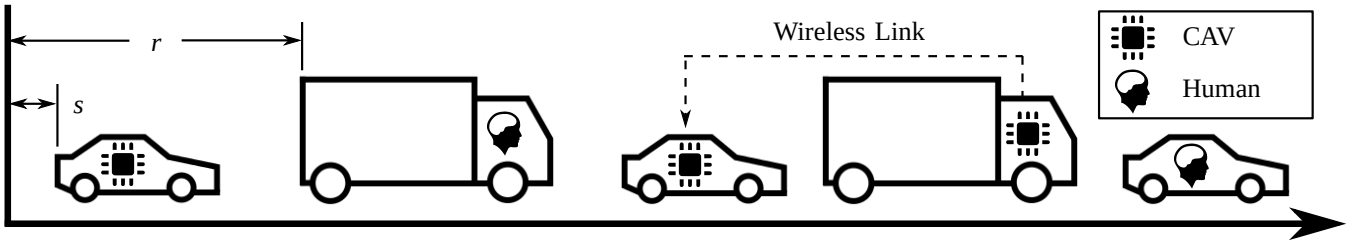

Fig. 1. Schematic of a heterogeneous vehicle string including both passenger and heavy vehicles, some of which are connected and automated. The position s of the ego vehicle and the position r of the preceding vehicle are shown considering the far left vehicle as the ego.

Especially in mixed traffic with unconnected vehicles, external learning and prediction of vehicle motion can improve performance. McDonough et al. used a Markov chain to predict vehicle speed and road grade as stochastic variables [20]. To predict 2D motion through intersections, Tran and Firl [21] applied Gaussian process models based on position to predict velocity. In contrast, Schepmann and Vahidi [22] showed performance improvement using a heuristic approach that predicts exponentially decaying powertrain torque.

This paper will present techniques for controlling connected and automated vehicles (CAVs) in a mixed traffic environment such as the one depicted in Figure 1. It begins with the vehicle dynamic and fuel consumption models of Section II that support anticipative control and simulation. Next, it progresses into algorithm design. While the core optimal control formulation drives performance improvements, it requires a preview of preceding vehicle (PV) motion. In partially-connected environments, this preview may or may not be directly available from the PV. Therefore, the controls discussion of Section III is followed by prediction methods tailored to each of these two cases in Section IV. The simulation scenario and baselines are described in Section V before the results are shown and discussed in Section VI. Finally, Section VII reviews contributions and envisions future research.

II. Modeling

A. Vehicle Kinematics

For optimization purposes, the standard linear model shown in Equation (1) represents longitudinal vehicular motion. This approximation enables the use of linear time-invariant (LTI) MPC. The continuous time model is discretized using the exact solution of the state equations. The position s, velocity v, and acceleration a of the ego vehicle compose the state vector and the acceleration command, denoted u, acts as an input that combines the powertrain and brake systems. A first-order lag with time constant τ separates the commanded and actual acceleration. While an experimental implementation would require a low-level acceleration controller, [23] shows such a controller's feasibility.

$$\begin{bmatrix} \dot{s} \\ \dot{v} \\ \dot{a} \end{bmatrix} = \begin{bmatrix} 0 & 1 & 0 \\ 0 & 0 & 1 \\ 0 & 0 & -\frac{1}{\tau} \end{bmatrix} \begin{bmatrix} s \\ v \\ a \end{bmatrix} + \begin{bmatrix} 0 \\ 0 \\ \frac{1}{\tau} \end{bmatrix} u \tag{1}$$

A strictly LTI model is not required for plant simulation, so further detail is included for this purpose. To model the differing dynamics of the powertrain and brake systems, the time constant used for simulation is selected based on the sign of the traction force F_t. The larger time constant τ_p models the slower powertrain while the smaller time constant τ_b represents the more responsive brake system. In passenger vehicles, $\tau_p = 0.45\,\text{s}$ and $\tau_b = 0.10\,\text{s}$. In heavy vehicles, $\tau_p = 0.90\,\text{s}$ and $\tau_b = 0.25\,\text{s}$. The mean of τ_p and τ_b is used for optimal control. This introduces mismatch between control and simulation models, but keeps the control model linear time-invariant.

$$\tau = \begin{cases} \tau_p & F_t \geq 0 \\ \tau_b & F_t < 0 \end{cases} \tag{2}$$

Compared to acceleration, traction force offers a more realistic means of time constant selection by capturing the effects of aerodynamic drag and friction on the boundary between braking and powertrain zones. The fuel consumption model of the following section conveniently includes the necessary force calculations.

B. Fuel Consumption

Because this controller seeks to reduce energy use among other objectives, fuel consumption modeling is a critical part of its development. The simulation tool continues to employ the modeling framework from [24]. This section reviews the model for convenience. First, Equation (3) determines the traction force F_t based on vehicle parameters (Table I), acceleration, and velocity. ρ_a denotes the density of air and g denotes the gravitational acceleration.

$$\begin{aligned} F_t =& m_{eff} a + \frac{1}{2} C_D \left(r - s - l_{veh}\right) \rho_a A_v v^2 \\ &+ \mu m g \cos\theta + m g \sin\theta \end{aligned} \tag{3}$$

The model then calculates the transmission output torque $T_{tr,o}$ and speed $n_{tr,o}$, again using parameters from Table I.

$$T_{tr,o} = F_t \frac{r_t}{r_f} \qquad n_{tr,o} = v \frac{r_f}{2\pi r_t} \tag{4, 5}$$

This demand on the powertrain determines the transmission gear using a precomputed lookup table. With the gear ratio known, engine speed and torque can be calculated and used to determine fuel rate from a second lookup table. The combined Newton's law and lookup table approach thus compensates for changes in road slope and vehicle mass, although these examples are both held constant here.

In an advancement over [24], the drag coefficient in Equation 3 depends upon the preceding vehicle's position r to account for slipstreaming. This phenomenon has been exploited

TABLE I
POWERTRAIN MODEL CONSTANTS.

Symbol	Definition	Light-Duty	Heavy-Duty
m	mass	1671 kg	19400 kg
m_{eff}	effective mass	1706.9 kg	19616 kg
l_{veh}	overall length	4.52 m	22 m
C_d	drag coefficient	0.29	0.544
A_v	frontal area	2.733 m^2	10.8 m^2
μ	friction coefficient	0.0150	0.0150
r_f	final drive ratio	3.21	4.88
r_t	tire radius	0.3454 m	0.60 m
a_{min}	braking capacity	-8.5 m/s^2	-6.0 m/s^2

TABLE II
POWERTRAIN MODEL RESULTS.

Cycle	EPA Label [MPG]	Model Result [MPG]
City	23	22.9
Highway	31	31.3

to improve fuel economy at steady speeds [25]. While the controller targets eco-driving rather than aerodynamic platooning, the simulation now captures any incidental slipstream effects on fuel economy — positive or negative. The drag coefficients of the ego vehicle depend on intervehicle gap according to Watkins and Vino [26] when following a passenger vehicle and Hucho [27] when following a heavy vehicle.

Additional brake specific fuel consumption (BSFC) mapping data from [28] was used to model heavy vehicle fuel consumption. Other parameters, including gear ratios, from [29], [30] for passenger vehicles and [31], [32] for heavy vehicles complete the model.

Because of readily available benchmark results from the U.S. Environmental Protection Agency (EPA), the accuracy of the passenger vehicle's fuel consumption model is reviewed here. Two vehicles were simulated in order to assess fuel economy on EPA cycles. The lead vehicle followed the cycles exactly without regard for operating point constraints. The second vehicle used the Intelligent Driver Model (IDM) described in Section V-A to follow the lead vehicle. The follower, which conforms to operating point constraints and incurs realistic speed error, was analyzed for fuel economy.

Using the formulas established in U.S. federal regulations [33], model-based city and highway fuel economy was calculated. Table II compares the results from the IDM-controlled following vehicle with the its EPA label.

III. Optimal Control Formulation

As Figure 1 indicates, the traffic streams considered herein may contain both heavy and passenger vehicles. Either vehicle type may be conventionally human-driven or connected and automated. The following two sections will develop methods of applying optimal control to either of these hardware types. Adding complexity, the preceding vehicle whose motion is anticipated can only provide its follower with an intent preview if that preceding vehicle is connected and automated. To handle the matrix of possible ego and preceding vehicle characteristics, we develop the four algorithm variants described in Table III. Further detail on in-horizon constraints, optimization types, the terminal constraint, use of connectivity, and the probability model can be found in Sections III-B, III-C, III-D, IV-A, and IV-B respectively. The control discussion begins with the objective.

A. Objective

In order to optimally balance acceleration smoothness with traffic compactness using a real-time capable problem formulation, the quadratic cost J of [24] is employed. This objective function penalizes acceleration and position error relative to the reference s_{ref} with weights q_a and q_g, respectively. Equation (7) determines the reference position relative to the anticipated PV position r_a using a calibrated target gap length d_{ref}. N denotes the prediction horizon.

$$J = q_g\left(s\left(N\right) - s_{ref}\left(N\right)\right)^2 + q_a a^2\left(N\right) + \sum_{i=0}^{N-1}\left[q_g\left(s\left(i\right) - s_{ref}\left(i\right)\right)^2 + q_a\left(a^2\left(i\right) + u^2\left(i\right)\right)\right] \tag{6}$$

$$s_{ref} = r_a - l_{veh} - d_{ref} \tag{7}$$

An alternative design might involve direct minimization of fuel consumption. Such optimizations can save fuel by accelerating from a stop efficiently and exhibiting pulse-and-glide behavior under free-flow cruise conditions [34]. Equation (6) is not capable of such performance. However, the direct fuel-minimizing design choice has drawbacks in this application. In addition to compromising ride comfort and disagreeing with surrounding drivers' expectations, pulse-and-glide can reduce or erase efficiency improvements by disrupting traffic flow [12]. Moreover, the true fuel consumption characteristic is nonlinear with respect to the measurable states in Equation (1). This results in a general nonlinear optimization that could increase computation time.

In contrast, the acceleration-minimizing approach in Equation (6) works to isolate upstream vehicles from jamming waves in traffic as demonstrated in [24]. Furthermore, the use of states from the linear model allows the problem to be formulated as a quadratic program (QP) or mixed integer quadratic program (MIQP)[1] for which fast commercial solvers exist. Acceleration minimization carries a risk of encouraging inefficient, that is, high BSFC engine operation, but this risk is mitigated by calibrating the penalty weights rigorously for good fuel economy. Section VI-B describes this process in greater detail.

B. In-Horizon Constraints

Output constraints prevent unsafe or illegal velocity and acceleration outside the vehicle's capability. The minimum velocity v_{min} prevents reversal and the maximum velocity v_{max} enforces speed limits. Maximum braking capacity is approximated as a constant u_{min}. In contrast, the powertrain's maximum acceleration capacity depends strongly on velocity. We approximate this complex limit using piecewise linear combinations of velocity and acceleration. Equations (10) and

[1]A mixed integer program involves both continuous and integer-valued decision variables.

TABLE III
ANTICIPATIVE ALGORITHM VARIANTS, FEATURES, AND APPLICATIONS.

Variant	Optimization	Preview Source	Worst-Case In-Horizon Constraint	Worst-Case Terminal Constraint	Application
NR-MPC	Quadratic Program	Connectivity	No	Yes	Passenger host following a CAV.
NR-MIPC	Mixed-Integer Quadratic Program	Connectivity	No	Yes	Heavy host following a CAV.
R-MPC	Quadratic Program	Probability Model	Yes	Yes	Passenger host following an unconnected vehicle.
R-MIPC	Mixed-Integer Quadratic Program	Probability Model	Yes	Yes	Heavy host following an unconnected vehicle.

(11) define these combined constraints where m and b are constants. Figures 2 and 3 illustrate the constraints below.

$$u_{min} \leq u \qquad v_{min} - \varepsilon_3 \leq v \leq v_{max} + \varepsilon_2 \qquad (8,\ 9)$$

$$-m_1 v + u \leq b_1 \qquad -m_2 v + u \leq b_2 \qquad (10,\ 11)$$

$$-m_1 v + a \leq b_1 + \varepsilon_4 \qquad -m_2 v + a \leq b_2 + \varepsilon_4 \qquad (12,\ 13)$$

In the passenger vehicle case, the two maximum acceleration lines have slopes $m = \{0.2850,\ -0.1208\}\,\mathrm{s}^{-1}$ and intersect at $(v,\ a) = (6.974\,\mathrm{m/s},\ 3.988\,\mathrm{m/s}^2)$. Their counterparts for the heavy vehicle have slopes $m = \{-0.20,\ -0.0238\}\,\mathrm{s}^{-1}$ and intersect at $(12.50\,\mathrm{m/s},\ 0.4974\,\mathrm{m/s}^2)$.

The output constraints include slack variables ε_i for softening. These slack variables multiplied by their respective penalties ρ_i add to the linear portion of the objective according to Equation (14). The augmented cost J_a is then minimized. To reduce the number of decision variables and enable formulation as a quadratic program [35], the slack variable cost J_ε uses the ∞-norm of each slack variable over the prediction horizon.

$$J_\varepsilon = \sum_{j=1}^{4} \rho_j \left|\left|\varepsilon_j\right|\right|_\infty \qquad J_a = J + J_\varepsilon \qquad (14,\ 15)$$

Depending upon the convexity of the acceleration-velocity constraint, Equations (10) and (11) along with the corresponding Equations (12) and (13) may be applied conjunctively or disjunctively. The conjunctive formulation results in a QP. The disjunctive formulation requires an MIQP and is discussed further in Section III-C.

Equation (16) ensures a safe gap $d_{min} > l_{veh}$ with the preceding vehicle at all stages. The constraint-oriented PV position r_c is set depending on algorithm variant and does not always equal r_a. In the robust formulations (R-MPC and R-MIPC), the worst-case position r_{wc} of the preceding vehicle is used. The standard formulations (NR-MPC and NR-MIPC) substitute the most likely i.e. the communicated PV position.

$$d_{min} - \varepsilon_1 \leq r_c - s \qquad (16)$$

$$r_c = \begin{cases} r_a & : \text{ NR-MPC, NR-MIPC} \\ r_{wc} & : \text{ R-MPC, R-MIPC} \end{cases} \qquad (17)$$

Determination of r_{wc} is discussed further at the close of Section IV-B.

C. Disjunctive Constraints and Mixed-Integer Programming

For general cruise control purposes that do not require the powertrain hardware's absolute maximum acceleration, the constraints of Equations (10), (11), (12), and (13) acceptably approximate a gasoline-powered vehicle's powertrain limitations as shown in Figure 2. The heavy diesel commercial vehicle, on the other hand, has a highly non-convex feasible region (Figure 3). Approximation using convex linear constraints results in severely restricted acceleration. To enable greater use of available torque at low vehicle speeds, we convert Equations (10), (11), (12), and (13) into disjunctive constraints using the Big M method [36]. This technique requires introduction of a binary decision variable β at each prediction step.

$$u - m_1 v - M\beta \leq b_1 \qquad (18)$$

$$a - m_1 v - M\beta \leq b_1 \qquad (19)$$

$$u - m_2 v - M(1-\beta) \leq b_2 \qquad (20)$$

$$a - m_2 v - M(1-\beta) \leq b_2 \qquad (21)$$

$$\beta \in \{0,1\} \qquad (22)$$

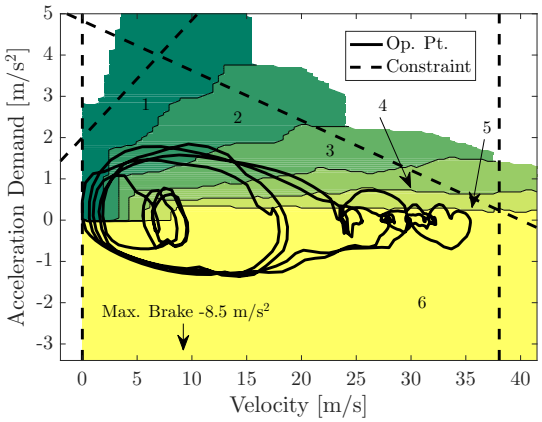

Fig. 2. Passenger vehicle gear map with conjunctive maximum acceleration constraints and sample US06 R-MPC operating point trace.

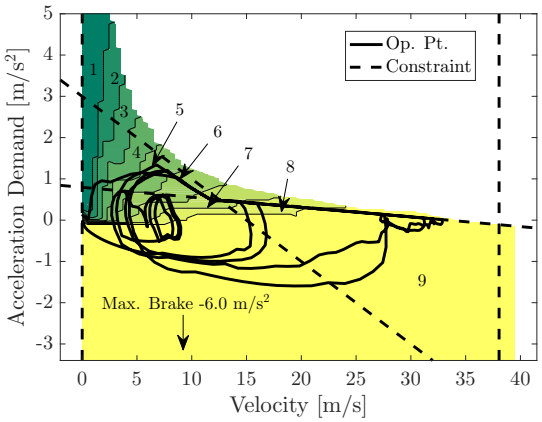

Fig. 3. Heavy vehicle gear map with disjunctive maximum acceleration constraints and sample US06 R-MIPC operating point trace.

This reformulation implies that although the MIQP will directly enforce Equations (18) AND (20), either Equation (10) OR (11) will hold. The same relationship applies to the parallel constraints on a. A standard MIQP formulation natively supports AND rather than OR logic in constraint enforcement, so the constraints are usable in this form.

Although the Big M method sometimes uses an arbitrarily large M, numerical issues can result from inexactness in β's integrality. Selecting the smallest suitable value of M limits numerical error in $M\beta$ and $M(1-\beta)$. In this problem with box constraints on v, M is computed as follows. Equation (23) takes the maximum difference between the constraint lines within the feasible velocity set.

$$M = \max \left\{ \begin{array}{l} m_2 v_{min} + b_2 - m_1 v_{min} - b_1, \\ m_2 v_{max} + b_2 - m_1 v_{max} - b_1 \end{array} \right\} \tag{23}$$

While this implementation uses two disjunctive constraints, the fundamental method can be extended to increase resolution at the cost of a higher number of binary variables. Even when using the first approximation presented in Figure 3, peak low-speed acceleration is approximately doubled compared to the higher-speed constraint alone[2]. This low-speed acceleration capability is important to help the heavy vehicles keep pace with passenger vehicles in traffic strings.

D. Terminal Constraint

Equation (16) prevents collisions during the model predictive controller's finite horizon. Such a system may still result in a collision if the prediction horizon length is insufficient. To address this concern, a terminal constraint limits a linear combination of the ego vehicle's position and velocity at the final stage of prediction. The overall strategy ensures that the ego vehicle can counter any PV control move to avoid a collision, even when the imminent collision would occur beyond the prediction horizon.

$$-m_3 v(N) + s(N) \leq \xi \tag{24}$$

The values of m_3 and ξ are calculated at each timestep from the constraint-oriented future PV state[3] using one-dimensional particle kinematics. To accommodate mixed traffic, we consider distinct minimum accelerations a_A of the PV and a_B of the ego vehicle. In the worst case, the preceding vehicle will apply maximum braking post-prediction. The most favorable action that the ego vehicle can take in this case is to apply its maximum braking effort. Hence we consider two particles, both with known acceleration. The lead particle's initial velocity v_{A0} is also known from step N of the constraint-oriented PV state trajectory. For an arbitrary positive initial distance between the particles, we seek an expression for the maximum velocity of the following particle v_{B0} such that the future gap never reaches zero. Using the relative reference frame fixed to the lead particle, we integrate the relative velocity of the following particle $v_{rel}(t)$ and subtract from the initial distance

[2]The higher-speed constraint cannot be freely adjusted because its root determines the maximum vehicle speed.

[3]The constraint-oriented future PV state may be either the anticipated one or a worst-case scenario. See Section IV for further detail on how these trajectories are calculated.

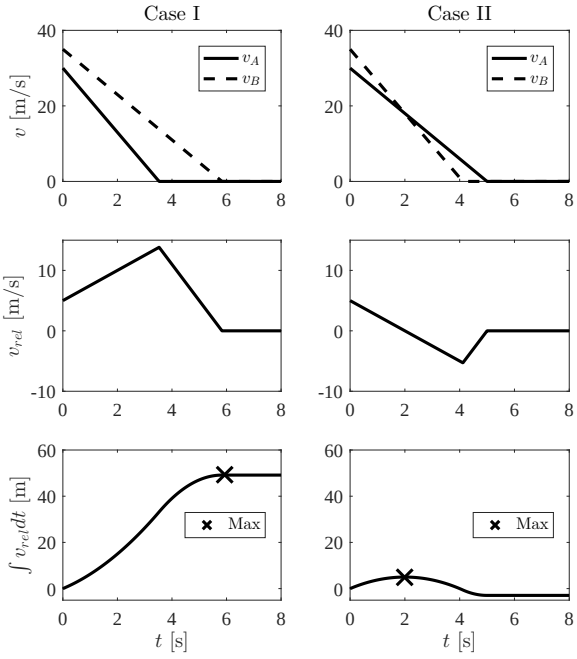

Fig. 4. Example post-prediction velocities, relative velocities, and integrated velocities for Case I (left) and Case II (right).

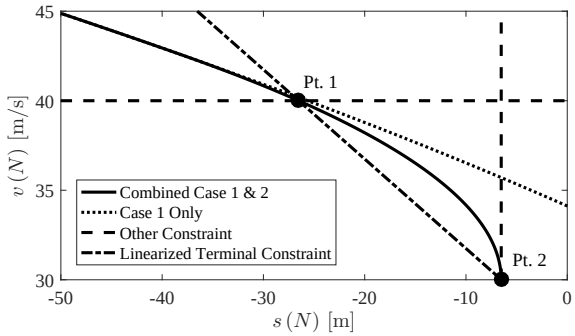

Fig. 5. The nonlinear terminal constraint and its linear approximation.

to find the distance at time t. Decreasing velocities saturate at zero, which can render $v_{rel}(t)$ piecewise. For example, the potentially dangerous case where the PV stops at time t_1 before the ego vehicle stops at time t_2 is described in Equation (26).

$$v_{rel} = v_B - v_A \tag{25}$$

$$v_{rel} = \left\{ \begin{array}{lll} (a_B - a_A)t + v_{B0} - v_{A0} & : & t_0 \leq t \leq t_1 \\ a_B t + v_{B0} & : & t_1 < t \leq t_2 \\ 0 & : & t > t_2 \end{array} \right. \tag{26}$$

Under some conditions, the integral of relative velocity must not exceed the initial gap at $t = \infty$. We will refer to this as Case 1.

$$\int_{t_0}^{\infty} v_{rel}\ dt \leq r(N) - d_{min} - s(N) \tag{27}$$

$$\int_{t_0}^{\infty} v_{rel}\ dt = \left[\frac{1}{2}(a_B - a_A)t^2 + (v_{B0} - v_{A0})t\right]_{t_0}^{t_1} + \left[\frac{1}{2}a_B t^2 + v_{B0}t\right]_{t_1}^{t_2} \tag{28}$$

$$\int_{t_0}^{\infty} v_{rel}\ dt = \frac{1}{2}\left(\frac{v_{A0}^2}{a_A} - \frac{v_{B0}^2}{a_B}\right) \leq r(N) - d_{min} - s(N) \tag{29}$$

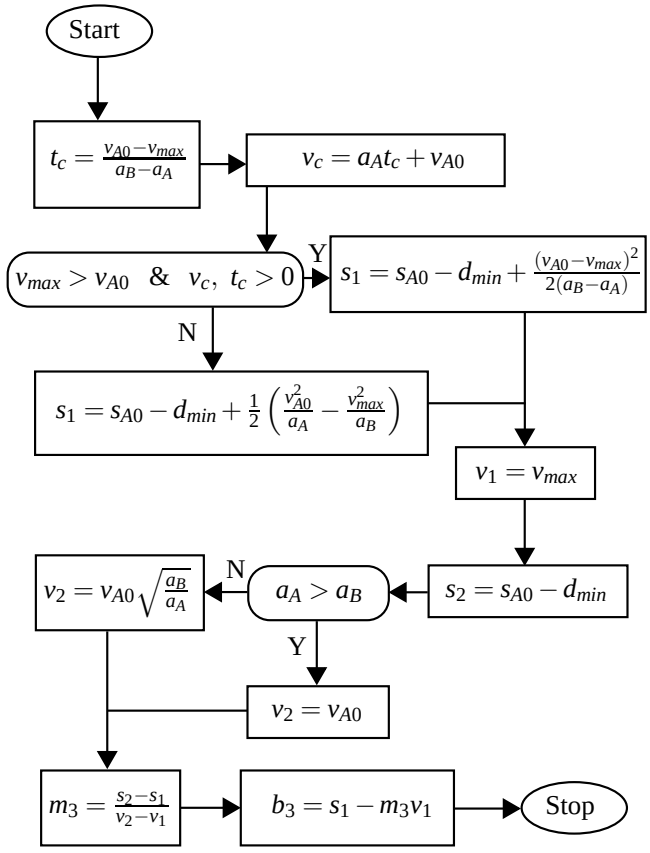

Fig. 6. Algorithm for online terminal constraint calculation.

In other cases, the above criterion is not sufficient to guarantee collision avoidance. Consider $a_A > a_B$, recalling that the signs of a_A and a_B are negative. Also let $v_{B0} > v_{A0}$. The maximum relative displacement, which coincides with $v_{rel} = 0$, may occur at a time $t_c < \infty$ if t_c is reached before the vehicles come to rest. We will refer to this as Case 2. To find the corresponding constraint, we first equate the velocities of the two particles to find t_c before using the result to integrate relative velocity. Figure 4 illustrates this section's integrals graphically where $t = 0$ at prediction step N.

$$a_B t_c + v_{B0} = a_A t_c + v_{A0} \tag{30}$$

$$t_c = \frac{v_{A0} - v_{B0}}{a_B - a_A} \tag{31}$$

$$max \int_{t_0}^{\infty} v_{rel}\ dt = \left[\frac{1}{2}(a_B - a_A)t^2 + (v_{B0} - v_{A0})t\right]_{t_0}^{t_c} \tag{32}$$

$$max \int_{t_0}^{\infty} v_{rel}\ dt = \frac{1}{2}\frac{(v_{A0} - v_{B0})^2}{(a_A - a_B)} \leq r(N) - d_{min} - s(N) \tag{33}$$

To linearize the constraint, we find a conservative linear approximation of Equations (29) and (33). Noting that the feasible region in (s, v) space is also bounded by simple maximum constraints on s and v and also that the nonlinear constraint is convex, we select the line passing through the points $(s_1, v_1 = v_{max})$ and $(s_2 = r(N) - d_{min}, v_2)$ as shown in Figure 5.

For points 1 and 2 in Figure 5, the appropriate case must be selected. We first turn our attention to point 1. Because v_1 is known, t_c can be determined immediately from Equation (31) and $v_B(t_c)$ follows from the particle's constant acceleration. Positive values of both t_c and v_c indicate that Case 2 applies. Otherwise, Case 1 is used.

Now, the correct case must be determined for point 2. In this case, $s_2 = r(N) - d_{min}$ and the maximum relative velocity integral is therefore 0. The more conservative case can be found by comparing the velocity result of Case 1 (Equation (34)) with that of Case 2 (Equation (35)). The result indicates that if the PV exceeds the braking capability of the ego vehicle, then Case 1 applies at point 2.

$$\frac{1}{2}\left(\frac{v_{A0}^2}{a_A} - \frac{v_{B0}^2}{a_B}\right) = 0 \implies v_{B0} = v_{A0}\sqrt{\frac{a_B}{a_A}} \tag{34}$$

$$\frac{1}{2}\frac{(v_{A0} - v_{B0})^2}{a_A - a_B} = 0 \implies v_{B0} = v_{A0} \tag{35}$$

$$v_{A0}\sqrt{\frac{a_B}{a_A}} < v_{A0} \iff |a_A| > |a_B| \tag{36}$$

Finally, slope and intercept calculations convert points 1 and 2 into the constraint given by Equation (24).

$$m_3 = \frac{s_2 - s_1}{v_2 - v_1} \tag{37}$$

$$\xi = s_1 - m_3 v_1 \tag{38}$$

Figure 6 shows the resulting algorithm, which is not limited by discrete timesteps and does not require numerical iteration.

IV. Preceding Vehicle Prediction

Both the objective and constraints require a prediction of future PV position and velocity. The prediction module anticipates the PV's control input vector u_a over the prediction horizon and uses the kinematic model of Equation (1) to predict the resultant PV states. Because the model is used to generate the final output, this approach always gives physically realistic trajectories. The following sections focus on the generation of u_a and r_a. They will also discuss calculation of r_{wc} where applicable. Section IV-A describes the method used when following a connected vehicle and Section IV-B describes the method used when following a conventional vehicle.

A. Intent Communication and Packet Loss Management

When the preceding vehicle uses MPC, it generates a full control input vector U^*_{PV} from each optimization. This vector is taken as u_a.

$$u_a = U^*_{PV} \tag{39}$$

Each CAV computes its optimal state trajectory according to Equation (1) and communicates it to the following vehicle. This includes its intended position r_a. In the full communication case, the trajectory is known with high certainty and we let $r_c = r_a$.

In reality, V2V connections suffer from packet loss that can cause the PV trajectory update to momentarily fail. In such an event, the following heuristic provides a substitute. The CAV stores the previous step's PV state trajectory in memory. If a packet is lost, the CAV's sensors can still measure the PV's new position $r(k)$ and use its progress to offset the previous loop's trajectory. Recall that r_a is a vector over time and r is a scalar.

$$r_a(k) = r_a(k-1) + (r(k) - r(k-1))\,[1, 1, \ \ldots \ 1] \tag{40}$$

Equation (40) assumes that the PV's intended acceleration profile undergoes only small changes over the course of a packet loss event and the most critical quantity to update is the current position. Compared to an alternative that advanced the previous loop's trajectory by one timestep, this strategy resulted in lower-jerk performance.

B. Preview Generation with Limited Information

In contrast to CAVs, conventional vehicles do not communicate data over the air and instead rely on visual signals. In the longitudinal dimension, this leaves the brake light as an acceleration command indicator. For compatibility with such vehicles, an extension to the probability model described in [24] is needed. The prior algorithm assumed that the PV communicated its current control input as one of $n_{bin,t} = 3$ discrete categories or *bins*: either accelerating, cruising, or braking. The ego vehicle then recursively learned a three-dimensional transition probability matrix P with elements P_{jhl}. P_{jhl} represented the probability that a PV control input l steps in the future would belong to bin h if the current input was in bin j. The concept of a strength matrix M that stores the total number of samples for each input state and timestep was introduced. This enabled reconstruction of the total number of samples at each step before incrementing this number in a counting-type scheme. The same concept is used to learn the transition matrix for this section's model.

Each acceleration command bin was characterized as its median value u_h with units of acceleration and the expected PV acceleration command l steps ahead $u_a(l)$ resulted from the following computation. Equation (41) is a weighted average that pulls the expected value toward a likely bin's median.

$$u_a(l) = \sum_{h=1}^{n_{bin,t}} u_h P_{jhl} \tag{41}$$

Rather than relying upon a braking, cruising, or acceleration indicator as in the prior work, the revised algorithm estimates the preceding vehicle's acceleration command $\hat{u}$ non-causally and predicts future PV acceleration commands based on sensed PV brake light state and velocity. Figure 7 describes the system architecture. 2 brake light bins and 3 discrete velocity bins divide the input space into 6 total regions. 5 discrete acceleration bins partition the target space into heavy braking (under $-2\,\mathrm{m/s^2}$), moderate braking ($-2\,\mathrm{m/s^2}$ to $-0.8\,\mathrm{m/s^2}$), cruising ($-0.8\,\mathrm{m/s^2}$ to $+0.8\,\mathrm{m/s^2}$), moderate acceleration ($+0.8\,\mathrm{m/s^2}$ to $+2.0\,\mathrm{m/s^2}$), and heavy acceleration (over $+2.0\,\mathrm{m/s^2}$). Each of these bins has a characteristic acceleration value u_h. These values are, in order from braking to acceleration, $\{-3.0, -1.4, 0, +1.4, +3.0\}\,\mathrm{m/s^2}$.

In contrast to [24], the number and definition of the discrete target bins are no longer linked to those of the input. This development is critical to accurately predicting the PV acceleration command when only the two-level brake light input is available.

The algorithm's online process is now described. First, the three most recent PV velocities are recorded in an array. Using these three measurements, the estimated acceleration at the previous step $\hat{a}(k-1)$ is calculated by applying a symmetric moving average filter to two finite difference time derivatives of velocity. The controller then estimates the PV control input from one step ago $\hat{u}(k-1)$ using Equation (42). In this section, A_{mn} and B_m refer to the element in row m and column n of the A and B matrices in the discretized state-space model of the form $x(k+1) = Ax(k) + Bu(k)$.

$$\hat{u}(k-1) = \frac{v(k) - v(k-1) - A_{23}\hat{a}(k-1)}{B_2} \tag{42}$$

Let $\lambda \in \{0, 1\}$ denote the PV brake light state, which is on for $F_t < 0$ [4] or $v = 0$. λ is stored in an array that contains $\lambda(k-N-1, k-N, \ \ldots \ , k-1)$. The PV velocity is binned into the near-stopped (under $1.6\,\mathrm{m/s}$), transition ($1.6\,\mathrm{m/s}$ to $28\,\mathrm{m/s}$), or cruising (over $28\,\mathrm{m/s}$) category and placed in an identically sized array. This binned velocity is denoted ν. Given these two input arrays of λ and ν over time, $\hat{u}(k-1)$ can be used to update the transition matrix at all timesteps during prediction. Because of the additional model input relative to [24], the transition matrix P now has four dimensions. The element $P_{\lambda\nu hl}$ stores the probability that, given current PV brake light state λ and velocity bin ν, the PV will command a desired acceleration within bin h at prediction step l. The strength matrix M, which is used to store the total number of data points encountered for a given set of input bins, has the three dimensions of λ, ν, and l. Element $M_{\lambda\nu l}$ of M stores the total number of learned l-step-ahead transitions with starting inputs λ and ν. The following steps describe the process of updating one element of P and M.

1) Reconstruct the number of samples for the current transition: $n_{\lambda\nu hl} = P_{\lambda\nu hl} M_{\lambda\nu l}$
2) Increment $n_{\lambda\nu hl}$
3) Increment the strength $M_{\lambda\nu l}$
4) Compute the new transition probability: $P_{\lambda\nu hl} = \frac{n_{\lambda\nu hl}}{M_{\lambda\nu l}}$

[4] This dependence on traction force and, in turn, aerodynamic drag causes the brake light's acceleration threshold to decrease as a function of velocity.

These steps are executed for each available time leap from an index of the λ and ν arrays to the most recent $\hat{u}$ data point.

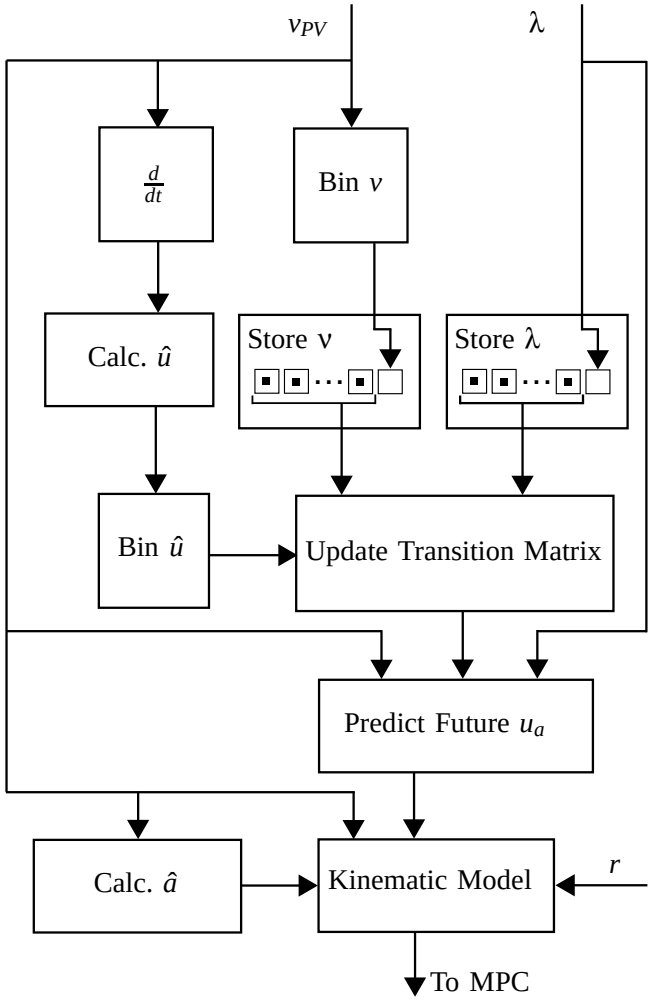

Fig. 7. Algorithm for generating the future PV position.

Future u values are computed similarly to Equation (41) based on bin probabilities. After a calibratable number of steps, the model no longer provides a benefit as shown in Section VI-A and is replaced with the assumption of $u = 0$. Repeated application of the kinematic model of Equation (1) to the current PV state then gives the anticipated PV position r_a. The initial PV acceleration $a(k)$ is not assumed to be measured and is estimated from the state equation as follows.

$$\hat{a}(k) = A_{33}\hat{a}(k-1) + B_3\hat{u}(k-1) \tag{43}$$

In summary, the resulting PV position trajectory depends upon the probability model output for near-future prediction; hence the predicted acceleration generally varies during this period. At more distant timesteps where the PV's control move becomes less related to its current state, zero acceleration command is assumed. This approximates constant velocity.

In the unconnected PV case, u_a is only known probabilistically and may be inaccurate during relatively rare events. To achieve robustness against all potential PV moves, the worst-case PV control input u_{wc} is set as follows. In an experimental implementation, the ego vehicle could estimate a worst-case value of u_{min} based on sensed PV type.

$$u_{wc} = [u_{min},\ u_{min},\ \ldots,\ u_{min}] \tag{44}$$

Equation (1) then gives the worst-case PV position r_{wc} based on u_{wc}. In contrast to the complete communication case, we let $r_c = r_{wc}$ because of the greater risk of incorrect prediction.

V. Simulation Methods

Eight vehicles follow a lead vehicle that tracks a predetermined velocity disturbance in an open-loop manner. The lead vehicle is *not* connected unless otherwise stated. This study uses the EPA US06 cycle [37] for its mixture of heavy and mild excitation. [24] found the US06 to occupy a middle ground between the stop-and-go city driving of the Federal Test Procedure (FTP) and the highway driving of the Highway Fuel Economy Test (HWFET). Each vehicle initializes with one vehicle length between its front bumper and its PV's rear bumper. Vehicles deactivate when they come to rest behind a deactivated PV. Deactivated vehicles do not move, consume fuel, or calculate new control inputs.

A. The Intelligent Driver Model as a Baseline

The Intelligent Driver Model (IDM) represents human drivers in the present simulations. While it can be used in reactive ACC [38], the inventors of the IDM used it to replicate phenomena observed in human drivers [39]. A study comparing the IDM to 12 other traffic models in its ability to predict travel times found the IDM to be one of the two best [40]. The model evaluation results in [41] supported this finding. Desired gap d_{des} and desired acceleration a_{des} result from the following closed-form structure [39]. Table IV shows the nominal parameters and their physical interpretations.

$$d_{des} = d_0 + max\left(0, \tau_h v + \frac{v\ \Delta v}{\sqrt{4a_0 b_0}}\right) \tag{45}$$

$$a_{des} = a_0\left[1 - \left(\frac{v}{v_0}\right)^{\delta} - \left(\frac{d_{des}(v,\ \Delta v)}{d}\right)^2\right] \tag{46}$$

TABLE IV
Mean intelligent driver model parameters.

Symbol	Definition	Light-Duty	Heavy-Duty
d_0	Minimum distance	10 m	13.6 m
τ_h	Minimum safe time headway	1.02 s	1.42 s
a_0	Maximum acceleration	1.52 m/s^2	1.14 m/s^2
b_0	Comfortable deceleration	3.24 m/s^2	2.29 m/s^2
δ	Acceleration exponent	4	4
v_0	Desired velocity	38.1 m/s	38.1 m/s

The authors' prior work in [24] set IDM parameters for operating space parity with MPC. This paper focuses more heavily on replicating human drivers. In accordance with this philosophy, systematically-determined parameters from [41] are drawn upon to more closely match human driver behavior. These results provide IDM parameter histograms representing a range of real driving styles. Here, the lognormal distributions of Figure 8 approximate these histograms using maximum

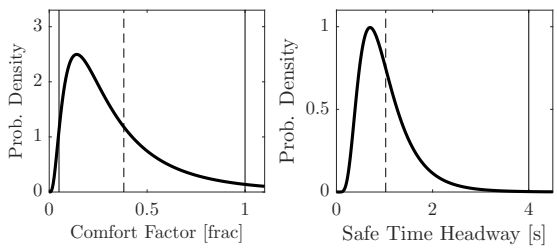

Fig. 8. Truncated lognormal distributions used to select the comfort factor *CF* (left) and desired time headway τ_h (right) for the baseline Intelligent Driver Model with mean values indicated in dashed lines. Solid hairlines mark truncation boundaries.

likelihood estimation. The *comfort factor*, denoted *CF*, is proposed as a method of linking the driver acceleration and braking intensity preferences a_0 and b_0.

$$a_0 = CF \cdot a_{max} \qquad b_0 = CF \cdot u_{min} \qquad (47,\ 48)$$

In Equation (47), a_{max} is the overall maximum acceleration value allowed in the appropriate powertrain operating envelope (either Figure 2 or Figure 3).

The results of Aghabayk et al. [42] show that heavy vehicles generally follow with longer distance and time headways compared to passenger vehicles. In a simplified adjustment, 0.4 s is added to heavy vehicle headways. Li et al. [43] provides heavy truck parameters for a quadratic car following model, which like the IDM uses a minimum distance. Compared to the conventional minimum distance in [39], Li's result suggests adding 3.6 m to d_0 for the heavy vehicle. To minimize the number of IDM collisions and collect more usable and meaningful fuel consumption data, the minimum distance d_0 was increased relative to conventional values.

B. Vehicle Type Variation

According to a 2015 U.S. Federal Highway Administration (FHWA) report, the most truck-concentrated portions of the U.S. National Highway System accommodate over 25% heavy traffic [44]. To simulate such an environment, a quasi-random selection of 0, 1, or 2 of the 8 following vehicles are set as heavy. A quasi-random sequence, also known as a low-discrepancy sequence, fills a space with points more uniformly compared to a true random sequence [45]. Specifically, we employ the Sobol sequence given by the MATLAB commands *sobolset* and *scramble* before rounding to integer values.

The penetration rate of connected and automated vehicles equipped with the proposed algorithm is varied from 0 to 100 percent. For each CAV count, the positions are varied using the same quasi-random method as the heavy vehicle placement algorithm. Figure 9 provides an example of a resulting simulation plan. This particular case requires 3 quasi-random variables: the queue index of the first CAV relative to the leader, the queue index of the second CAV relative to the first CAV, and the queue position of the heavy vehicle. The three-dimensional space is represented using 3 two-dimensional projections. Sequence outputs that result in vehicle placement outside the 8-vehicle string are disallowed and replaced with the next feasible output. For example, if the first CAV is in position 7 and the second CAV is 5 indices behind it, the second CAV is in position 12, outside of the 8-vehicle string.

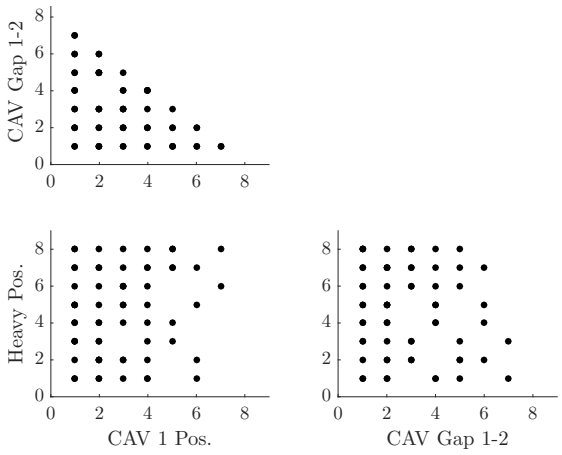

Fig. 9. Projections of the simulation plan for the case with 1 heavy vehicle and 2 CAVs.

Assignment of algorithm variants to vehicles depends on ego and preceding vehicle type according to Table III.

C. Packet Loss

Especially at higher CAV penetration rates, packet loss potentially becomes an important factor in connected control performance as mentioned in Section IV-A. Wang et al. [46] measured the percentage of transmitted packets that were received, or packet delivery rate (*PDR*), while using an IEEE 802.11p system in a variety of scenarios . The simulations in this paper randomly lose packets with distance-dependent probability according to a linear regression of the findings in [46]. This anticipative cruise control algorithm requires one-way communication with the vehicle immediately ahead, so the one-way communication case with line-of-sight is considered. Equation (49) gives the linear rule for *PDR* as a percentage.

$$PDR = -0.09197\,(r-s) + 99.43 \qquad (49)$$

VI. Simulation Results

A. Prediction Model

The prediction model described in Section IV-B contains three major subfunctions.

1) Estimate the past PV control inputs.
2) Predict the future PV control inputs.
3) Predict the future PV position resulting from its future control inputs.

Figure 10 demonstrates capability to accomplish function 1. The residuals relative to assuming $u = 0$ are shown in Figure 11, which indicates the time range over which the probability model assists in function 2. Figure 12 presents the correlation of function 3 for the prediction model's time range as well as the entire prediction horizon. Finally, Figure 13 gives the percentage of points that fall within a desired error boundary at various 1.0 s prediction timesteps. The PV for this section's results used the mean IDM parameters and followed immediately behind the lead vehicle. Learning was

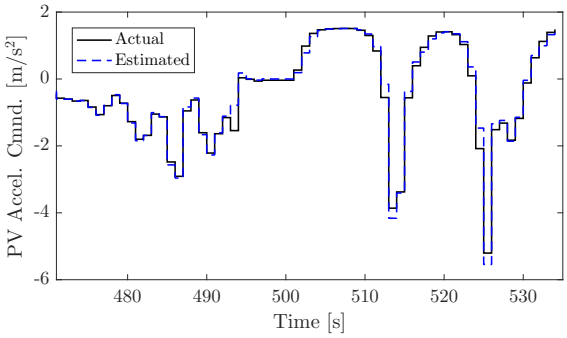

Fig. 10. Comparison of actual and estimated PV u over a cycle segment.

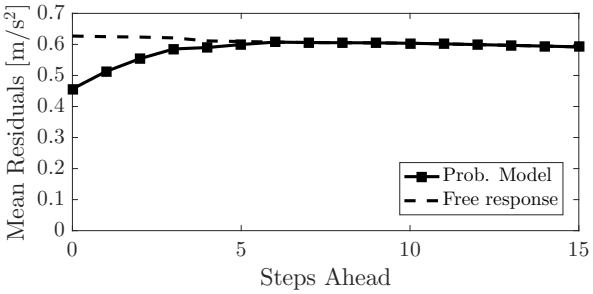

Fig. 11. Mean PV u residuals of the prediction algorithm after one cycle.

active during simulation and did not warm-start with past data.

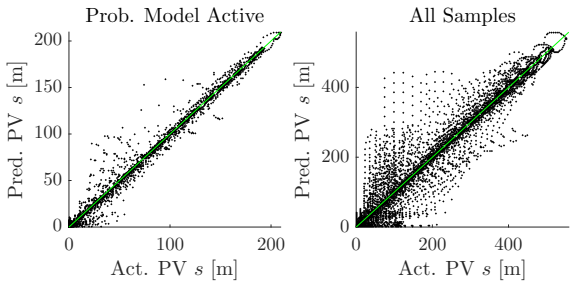

Fig. 12. Combined probability and kinematic model result for PV position prediction. Performance during the first 6 steps when the probability model is active (left) is compared with overall performance for the 16 s prediction horizon (right).

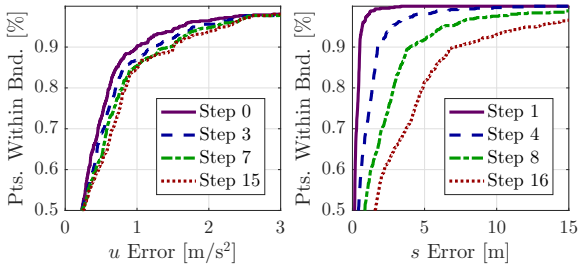

Fig. 13. Percentage of points meeting maximum error criteria in u and s at various prediction stages.

B. Parameter Calibration

As mentioned in Section III-A, proper calibration helps the anticipative cruise control algorithm achieve its best performance. To this end, a parameter optimization was performed to

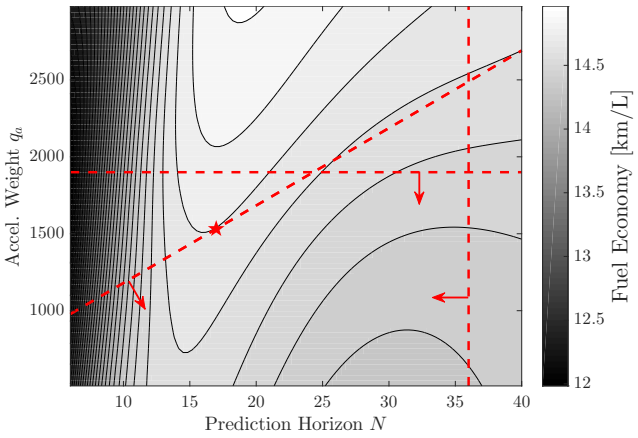

Fig. 14. Fuel consumption contours used to calibrate the NR-MPC algorithm. Constraints in the input domain are established to prevent collisions, limit computation time, and avoid excessive following distances and travel times compared to human drivers.

find optimal values of the weight q_a and the prediction horizon N. This effort improves on the methods and results presented in [24] by moving from a one-factor-at-a-time approach to a more global optimization. In a further advancement relative to [24], the full calibration process was performed for all MPC algorithm variants. The procedure is summarized as follows.

1) Generate a quasi-random sequence of trial parameter sets (N, q_a) that fills a box in R^2.
2) Simulate controllers using each trial parameter set.
3) Model the responses with a continuous function.
4) Define constraints to exclude parameter combinations with excessive space utilization, trip completion time, or computation time.
5) Select the parameter set that maximizes fuel economy subject to the constraints in 4. If the problem is not bounded within the box from 1, repeat 1 with a larger box and repeat the process.

To simulate a calibration testbed with minimal resources, a single vehicle rather than a string was used to collect calibration data during Item 2. This is also a self-serving strategy that optimizes performance of the ego vehicle given a certain PV behavior pattern without regard for the efficiency of upstream followers. The question of whether optimization based on a string of vehicles gives an overall traffic benefit remains open for future research.

Figure 14 presents a sample fuel economy maximization problem and its graphical solution. The resulting calibrations are shown in Table V.

C. Single-Vehicle Fuel Economy Verification

Since the calibration process relies on surface fitting, the selected calibrations are verified in direct simulation. Fuel economy results for an individual vehicle are presented in Figure 15. The connected CAVs in this dataset experienced packet loss.

The connected case in Figure 15 shows a 24.6 % fuel economy benefit over the human-like IDM in passenger vehicles and a 12.3 % fuel economy benefit in heavy vehicles. For comparison, [47] achieved 17.2 % fuel economy improvement

TABLE V
CALIBRATION RESULTS.

Algorithm	Parameter	Value
NR-MPC	N	17
	q_a	1530
R-MPC	N	16
	q_a	850
NR-MIPC	N	22
	q_a	4000
R-MIPC	N	12
	q_a	1330

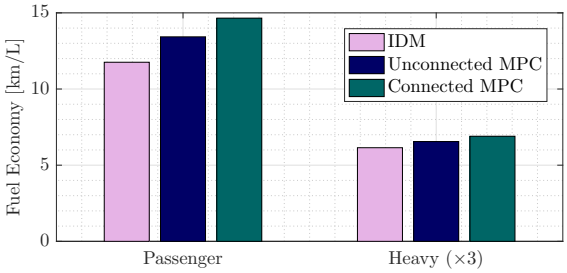

Fig. 15. Single-vehicle fuel economy results comparing the MPC cruise control system to a human-like IDM baseline. Heavy vehicle results are multiplied by 3 for visibility.

over a PI controller using a fuel-minimizing approach in a similar context. That result used a modified form of the FTP cycle in which [24] found a greater benefit of anticipative cruise control compared to the US06 that is used here.

D. Computation Time

Table VI shows the as-calibrated computation times for each algorithm variant. The simulation plan featured one open-loop vehicle and the vehicle of interest. Preview was provided to the R-MPC and R-MIPC vehicles, but not to the NR-MPC or NR-MIPC vehicles. The test computer was a laptop PC equipped with 16.0 GB RAM and a 2.70 GHz CPU. In Table VI, Opt. Time refers to the time required to solve the mathematical program (QP or MIQP) and Ctrl. Time refers to the total time required to run a single vehicle's control move determination, including both preview handling and optimization.

TABLE VI
COMPUTATION TIME.

Algorithm	Mean Ctrl. Time [s]	Max Ctrl. Time [s]	Mean Opt. Time [s]	Max Opt. Time [s]
NR-MPC	0.0337	0.0561	0.0108	0.0444
R-MPC	0.0757	0.1134	0.0110	0.0892
NR-MIPC	0.0435	0.0789	0.0148	0.0504
R-MIPC	0.0571	0.0919	0.0069	0.0425

E. Results by String Composition

The results of the 2224-simulation run outlined in Section V-B are shown in Figures 16, 17, and 18. Each data point represents the average of a set of simulations with common string composition but diverse vehicle arrangements and IDM parameters. A comparison between homogeneous human-like IDM strings and those composed entirely of CAVs is available from the endpoints of Figures 16, 17, and 18.

Acceleration, which the cost function directly penalizes, generally decreased with increasing CAV penetration rate as expected. While the presence of heavy vehicles reduced overall acceleration, CAVs provided a benefit regardless of the string's vehicle type makeup. Fuel economy also improved with an approximately linear trend as CAV penetration rate was increased. The percentage improvement in fleet fuel economy per unit increase in CAV penetration rate decreased somewhat with the introduction of heavy vehicles. Nonetheless, a significant improvement of around 1.4% fuel economy per 10% increase in CAVs still held with 2 of 8 vehicles as heavy trucks. This suggests that some traffic improvement from CAVs will apply regardless of regional or temporal differences in traffic composition.

We note a reduction in anticipated fuel economy improvement relative to the US06 results in [24]. Several factors contribute to this results change, the most important of which being the targeting of IDM parameters to match human driver behavior rather than the MPC constraints. Other changes that directionally improved IDM fuel economy relative to that of MPC include randomization of IDM parameters, powertrain model updates, mixing of R-MPC with NR-MPC, the use of nonzero vehicle length, and relaxation of the overall maximum braking constraint. Moreover, the results in Figures 16, 17, 18 do not assume that the lead vehicle that drives the disturbance is connected as in [24].

In contrast to the acceleration and fuel economy results of Figures 16 and 17, the space utilization trend is bimodal as penetration rate increases (Figure 18). At lower CAV penetration rates, CAVs are more likely to follow conventional vehicles and employ R-MPC or R-MIPC to guarantee collision avoidance. This worsens space utilization. As CAVs become highly concentrated, they are more likely to follow a CAV PV and use NR-MPC or NR-MIPC, improving space utilization [24]. This result is related to the present algorithm designs and selection strategy. By accepting some collision risk as humans do, the control designer may reduce CAV space utilization, especially at lower penetration rates.

The IDM tends to avoid collisions because of a singularity as current intervehicle gap approaches zero. However, collisions may occur when braking saturates. Indeed, a pair of IDM vehicles collided in this dataset while the CAVs were collision-free. An advantage of MPC for this application is its ability to guarantee collision avoidance even in the presence of braking constraints.

VII. CONCLUSIONS AND FUTURE WORK

An MPC-based cruise control algorithm for CAVs has been extended for control of widely differing hardware. This goal is accomplished by employing MIQP to optimize control of vehicles with non-convex operating regions. A constraint on the terminal set that guarantees collision avoidance analytically among vehicles with differing minimum accelerations has been described. Moreover, the PV prediction algorithm has been adapted for interaction with conventional vehicles.

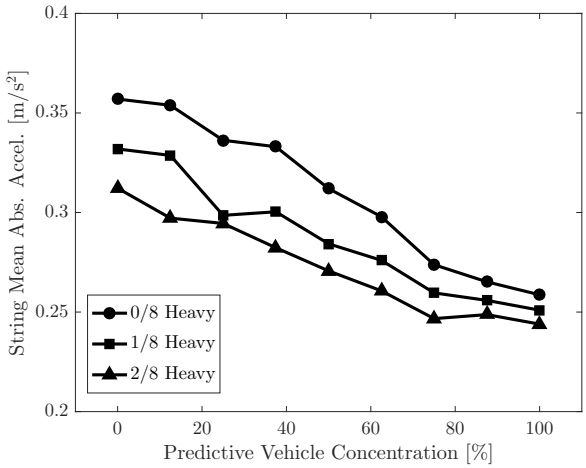

Fig. 16. Overall string acceleration results at various concentrations of predictive and heavy vehicles.

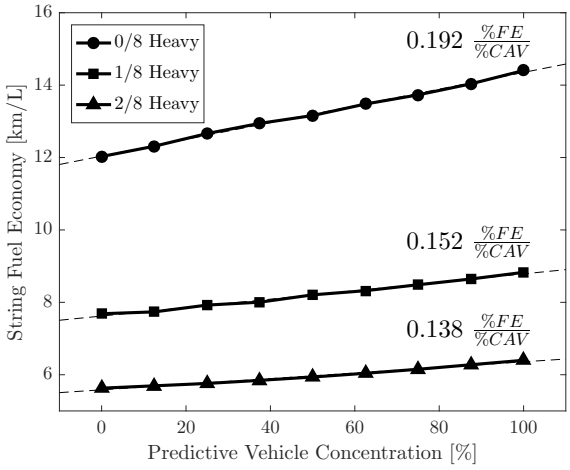

Fig. 17. Overall string fuel economy results at various concentrations of predictive and heavy vehicles.

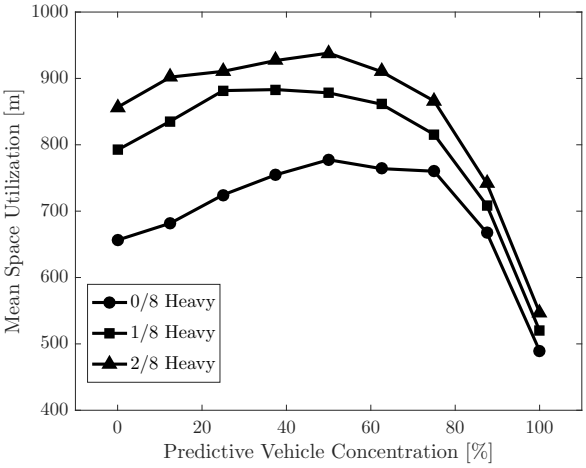

Fig. 18. Overall string space utilization results at various concentrations of predictive and heavy vehicles.

The resulting system was calibrated using an offline global optimization.

The proposed algorithms have been validated extensively in simulation with 2224 trial cycles involving 8-vehicle strings. Heavy vehicle concentrations of 0%, 12.5%, and 25% were simulated with quasi-random placement of heavy vehicles and CAVs. CAV penetration rate was varied from 0% to 100%, with human behavior modeled using the IDM with pseudorandom parameters. Simulated V2V communication was subject to random packet loss. Results show consistent fleet fuel economy improvements of 1.4% to 1.9% per 10 percentage point increase in CAV concentration. The entire validation dataset was collision-free for MPC vehicles, confirming the theoretical safety guarantees.

The realism of the results herein is limited by the single-file scenario and prescribed lead vehicle velocity trace. While braking events due to phantom jamming waves, cut-ins, and slowing PV's can certainly be mitigated with intelligent longitudinal driving, others that arise due to stop signs or similar rules cannot. This motivates a more complex simulation framework that integrates the full traffic ecosystem in order to fully understand the impact of ITS. In such an environment, optimal lane change control could result in further efficiency and safety improvements. Therefore, future work will target coupling of the longitudinal and lateral dimensions for intelligent motion control in multi-lane traffic. Experiments involving interaction between real and simulated vehicles are also planned.

VIII. Acknowledgement

This research was supported in part by an award from the U.S. Department of Energy Vehicle Technologies Office (Project No. DE-EE0008232).

References

[1] L. Blincoe, T. R. Miller, E. Zaloshnja, and B. A. Lawrence, "The economic and societal impact of motor vehicle crashes, 2010 (revised)," NHTSA, Washington, DC, NHTSA Tech. Rep., 2015.

[2] IIHS Highway Loss Data Institute. (2016) Fatality facts. [Online]. Available: http://www.iihs.org/iihs/topics/t/general-statistics/fatalityfacts/state-by-state-overview

[3] European Commission. (2017) Road safety: Encouraging results in 2016 call for continued efforts to save lives on EU roads. [Online]. Available: http://europa.eu/rapid/press-release_IP-17-674_en.htm

[4] NHSTA, "Traffic safety facts 2015," U.S. Dept. of Transportation, Washington, DC, NHTSA Tech. Rep., 2015.

[5] Delphi. (2015) Delphi adaptive cruise control. [Online]. Available: https://www.delphi.com/docs/default-source/old-delphi-files/7705dce6-d83a-45b7-b378-bd3f732c76e0-pdf

[6] B. Romans. (2016, June) 2016 Honda Civic: Highway cruising with adaptive cruise control and lane departure intervention. Edmunds. [Online]. Available: https://www.edmunds.com/honda/civic/2016/long-term-road-test/2016-honda-civic-highway-cruising-with-adaptive-cruise-control-and-lane-departure-intervention.html

[7] Ryan Beene. (2017) Self-driving car accidents: Robot drivers are odd, and thats why they get hit. The Seattle Times. [Online]. Available: https://www.seattletimes.com/business/self-driving-car-accidents-robot-drivers-are-odd-and-thats-why-they-get-hit/

[8] Associated Press. (2016) Google self-driving car caught on video colliding with bus. The Guardian. [Online]. Available: https://www.theguardian.com/technology/2016/mar/09/google-self-driving-car-crash-video-accident-bus

[9] E. C. Baig. (2017) Uber halts self-driving car tests after Arizona crash. USA Today. [Online]. Available: https://www.theguardian.com/technology/2016/mar/09/google-self-driving-car-crash-video-accident-bus

[10] C. Dora, "A different route to health: implications of transport policies," *BMJ*, vol. 318, no. 7199, pp. 1686–1689, 1991.

[11] Federal Reserve Bank of St. Louis. (2017) Moving 12-month total vehicle miles traveled. [Online]. Available: https://fred.stlouisfed.org/series/M12MTVUSM227NFWA

[12] S. E. Li, K. Deng, Y. Zheng, and H. Peng, "Effect of pulse-and-glide strategy on traffic flow for a platoon of mixed automated and manually driven vehicles," *Comput.-Aided Civil and Infrastructure Eng.*, vol. 30, no. 11, pp. 892–905, 2015.

[13] R. E. Stern, S. Cui, M. L. D. Monache, R. Bhadani, M. Bunting, M. Churchill, N. Hamilton, R. Haulcy, H. Pohlmann, F. Wu, B. Piccoli, B. Seibold, J. Sprinkle, and D. B. Work, "Dissipation of stop-and-go waves via control of autonomous vehicles: Field experiments," *arXiv preprint arXiv:1705.01693*, 2017.

[14] G. Orosz, "Connected cruise control: Modelling, delay effects, and nonlinear behavior," *Vehicle System Dynamics*, vol. 54, no. 8, pp. 1147–1176, 2016.

[15] C. Zhang and A. Vahidi, "Predictive cruise control with probabilistic constraints for eco driving," in *ASME 2011 Dynamic Syst. and Control Conf. and Bath/ASME Symp. on Fluid Power and Motion Control*, vol. 2, no. DSCC2011-5982, 2011, pp. 233–238.

[16] M. A. S. Kamal, J. Imura, T. Hayakawa, A. Ohata, and K. Aihara, "Smart driving of a vehicle using model predictive control for improving traffic flow," *IEEE Trans. Intell. Transp. Syst.*, vol. 15, no. 2, pp. 878–888, 2014.

[17] S. Lefèvre, A. Carvalho, and F. Borrelli, "A learning-based framework for velocity control in autonomous driving," *IEEE Trans. on Automation Sci. and Eng.*, vol. 13, no. 1, pp. 32–42, 2016.

[18] W. B. Dunbar and D. S. Caveney, "Distributed receding horizon control of vehicle platoons: Stability and string stability," *IEEE Trans. on Automat. Control*, vol. 57, no. 3, pp. 620–633, 2012.

[19] S. Magdici and M. Althoff, "Adaptive cruise control with safety guarantees for autonomous vehicles," in *Proc. World Congr. Int. Federation of Automat. Control*, 2013.

[20] K. McDonough, I. Kolmanovsky, D. Filev, S. Szwabowski, D. Yanakiev, and J. Michelini, "Stochastic fuel efficient optimal control of vehicle speed," *LNCIS*, vol. 455, pp. 147–162, 2014.

[21] Q. Tran and J. Firl, "Modelling of traffic situations at urban intersections with probabilistic non-parametric regression," in *IEEE Intell. Veh. Symp.*, no. 4, 2013, pp. 334–339.

[22] S. Schepmann and A. Vahidi, "Ultracapacitor power assist with preview-based energy management for reducing fuel consumption of heavy vehicles," *Int. J. Powertrains*, in print, 2016.

[23] I. Ha, A. K. Tugcu, and N. M. Boustany, "Feedback linearizing control of vehicle longitudinal acceleration," *IEEE Trans. Automat. Control*, vol. 34, no. 7, pp. 689–698, 1989.

[24] R. A. Dollar and A. Vahidi, "Quantifying the impact of limited information and control robustness on connected automated platoons," in *IEEE Intell. Transp. Syst. Conf.*, 2017.

[25] A. A. Alam, A. Gattami, and K. H. Johansson, "An experimental study on the fuel reduction potential of heavy duty vehicle platooning," in *IEEE Intell. Transp. Syst. Conf.*, 2010.

[26] S. Watkins and G. Vino, "Ultracapacitor power assist with preview-based energy management for reducing fuel consumption of heavy vehicles," *J. Wind Eng. and Industrial Aerodynamics*, vol. 96, no. 6, pp. 1232–1239, 2008.

[27] W. H. Hucho, *Aerodynamics of Road Vehicles: From Fluid Mechanics to Vehicle Engineering*. Warrendale, PA: SAE Int., 1998.

[28] V. Turri, "Fuel-efficient and safe heavy-duty vehicle platooning through look-ahead control," Licentiate thesis, KTH Royal Inst. Technology, October 2015.

[29] Ford Motor Company. (2016) 2016 Ford Escape technical specifications. [Online]. Available: https://media.ford.com/content/fordmedia/fna/us/en/asset.download.document.pdf.html/content/dam/fordmedia/NorthAmerica/US/product/2016/2016-escape-tech-specs.pdf

[30] ——. (2017) 2016 Ford Escape crossover. [Online]. Available: http://www.ford.com/suvs-crossovers/escape/2016/models/escape-se/

[31] TREMEC. (2014) Medium and heavy duty transmission specifications. [Online]. Available: http://www.tremec.com/anexos/MD-HD%20Condensed%20Specs%20Brochure.pdf

[32] Dana. (2017) Spicer axle, driveshaft, tire-pressure management systems, and wheel-end systems specifications guide. [Online]. Available: www.dana.com/~/media/danacom/files/media-asset/aftermarket-files/aftermarket-batch-1/gs8tjtnn7euhdvpokconspec32014.pdf

[33] "Vehicle-specific 5-cycle fuel economy and carbon-related exhaust emissions calculations," §600.114-12, U.S. Government Publishing Office.

[34] S. Li and H. Peng, "Strategies to minimize the fuel consumption of passenger cars during car-following scenarios," *Proc. of the Institution of Mech. Eng., Part D: J. of Automobile Eng.*, vol. 226, no. 3, pp. 419–429, 2012.

[35] E. C. Kerrigan and J. M. Maciejowski, "Soft constraints and exact penalty functions in model predictive control," in *UKACC Int. Conf., Cambridge*, 2000. [Online]. Available: https://spiral.imperial.ac.uk/bitstream/10044/1/10241/6/cued_control_53.pdf

[36] C. Bilodeau. (2015) Disjunctive inequalities. [Online]. Available: https://optimization.mccormick.northwestern.edu/index.php/Disjunctive_inequalities

[37] U.S. Environmental Protection Agency. (2016, April) Dynamometer drive schedules. [Online]. Available: https://www.epa.gov/vehicle-and-fuel-emissions-testing/dynamometer-drive-schedules#vehicleDDS

[38] R. Malinauskas, "The intelligent driver model: Analysis and application to adaptive cruise control," Master's thesis, Clemson University, May 2014. [Online]. Available: http://tigerprints.clemson.edu/all_theses/1934/

[39] M. Treiber, A. Hennecke, and D. Helbing, "Congested traffic states in empirical observations and microscopic simulations," *Physical Review E*, vol. 62, no. 2, pp. 1805–1824, 2000.

[40] E. Brockfeld, R. Kühne, A. Skabardonis, and P. Wagner, "Toward benchmarking of microscopic traffic flow models," *Transportation Research Rec.: J. Transportation Research Board*, vol. 1852, no. 03-3164, pp. 124–129, 2003.

[41] M. Pourabdollah, E. Bjärkvik, F. Fürer, B. Lindenberg, and K. Burgdorf, "Calibration and evaluation of car following models using real-world driving data," in *Intelligent Transportation Systems (ITSC), 2017 IEEE 20th International Conference on*, 2017, pp. 1–6.

[42] K. Aghabayk, M. Sarvi, and W. Young, "Understanding the dynamics of heavy vehicle interactions in car following," *J. Transportation Eng.*, vol. 138, no. 12, pp. 1468–1475, 2012.

[43] S. Li, J. Wang, K. Li, X. Lian, H. Ukawa, and D. Bai, "Modeling and verification of heavy-duty truck drivers' car-following characteristics," *J. Transportation Eng.*, vol. 11, no. 1, pp. 81–87, 2010.

[44] M. Chambers, J. Goworowska, C. Rick, and J. Sedor, "Freight facts and figures 2015," U.S. Dept. Transportation, Bureau Transportation Stat., Washington, DC, Tech. Rep. 11, 2015.

[45] G. Levy, "An introduction to quasi-random numbers," Numerical Algorithms Group Ltd., Oxford, UK, Tech. Rep., 2011.

[46] Y. Wang, J. Hu, Y. Zhang, and C. Xu, "Reliability evaluation of IEEE 802.11p-based vehicle-to-vehicle communication in an urban expressway," *Tsinghua Science and Technology*, vol. 20, no. 03-3164, pp. 124–129, 2015.

[47] T. Stanger and L. del Re, "A model predictive cooperative adaptive cruise control approach," in *American Control Conference (ACC), 2013*, no. 4. IEEE, 2013, pp. 1374–1379.

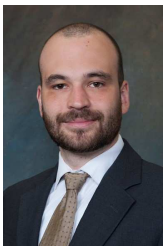

R. Austin Dollar holds a B.S. degree in mechanical engineering from Purdue University in West Lafayette, Indiana awarded in 2014. He is currently a Ph.D. student with the department of mechanical engineering at Clemson University in Clemson, South Carolina. Prior to joining Clemson University in 2016, he was a gasoline engine calibration specialist with General Motors Global Propulsion Systems and worked in the area of transient torque and boost control. His current research focuses on optimal control of automated and semi-automated vehicles including connectivity and eco-driving.

Ardalan Vahidi is a Professor of Mechanical Engineering at Clemson University, South Carolina. He received his Ph.D. in mechanical engineering from the University of Michigan, Ann Arbor, in 2005, M.Sc. in transportation safety from George Washington University, Washington, DC, in 2002, and B.S. and M.Sc. in civil engineering from Sharif University, Tehran in 1996 and 1998, respectively. In 2012–2013 he was a Visiting Scholar at the University of California, Berkeley. He has also held scientific visiting positions at BMW Technology Office in California, and at IFP Energies nouvelles, in France. His research is at the intersection of energy, vehicular systems, and automatic control. His recent publications span topics in alternative vehicle powertrains, intelligent transportation systems, and connected and autonomous vehicle technologies.